# Local Transitions in Flow Phenomena through Packed Beds Identified by MRI

**M. L. Johns, A. J. Sederman, A. S. Bramley, and L. F. Gladden**
Dept. of Chemical Engineering, University of Cambridge, Cambridge CB2 3RA, U.K.

**P. Alexander**
Dept. of Physics, University of Cambridge, Cavendish Laboratory, Cambridge CB3 0HE, U.K.

*Magnetic resonance imaging (MRI) velocity measurement techniques are used to investigate flow of water and a glucose solution, of viscosity $3.89 \times 10^{-3}$ Pa·s, within the interparticle space of a cylindrical packed bed of 5 mm diameter glass ballotini. The experiments were performed over a range of Reynolds numbers from 0.84 to 14.52, spanning the regime where inertial effects begin to play a significant role relative to viscous forces. A transition from creeping to inertial flow occurs in isolated pores at a local Reynolds number, defined for each pore within the interparticle space, of approximately 30. Despite this transition in flow behavior in some pores, the gross features of the flow pattern scale approximately with flow rate, which can be explained by considering the volume of the void space in which the flow is nearly stagnant as largely determining the pressure distribution within the bed.*

## Introduction

Describing the transport processes occurring within the void space of porous media is of fundamental importance to numerous scientific fields, ranging from reservoir engineering to the application of packed beds in chemical processes. Owing to their complexity, porous media are often treated as an effectively homogeneous system from which bulk properties of the flow are determined. This approach neglects the complexity of flow within the individual pores and constrictions which constitute a typical porous medium. Such local information is required to understand and describe completely any given physical process occurring within the system. A commonly encountered situation is that of laminar flow within the porous medium, where viscous effects dominate the transport (this is often referred to as the creeping flow regime) as well as transitions from this creeping flow regime as inertial forces become important as a result of changing flow rate and Reynolds number. An understanding of such phenomena is of relevance to flow phenomena within packed beds typically encountered in chemical reaction engineering, as well as single and multiphase flow phenomena within porous media such as rocks and soil. The aim of this study is to investigate the extent to which the transport of fluid through a porous medium scales with flow rate and, hence, Reynolds number, and the effect of the local structure of the void space, at the single pore level, on the local and global transport characteristics of the porous medium.

Magnetic resonance imaging (MRI) is now established as a probe of structure-transport relationships in porous media. The use of MRI to measure the spatial distribution of pore-scale flow in a porous system has utilized either a time-of-flight method (Nesbitt et al., 1991), or exploited a phase-shift encoding method (Rajanayagam et al., 1995; Kutsovsky et al., 1996). Time-of-flight methods were shown to give anomalous results due to magnetic susceptibility effects between the liquid and solid phases, a limitation avoided by the phase-shift encoding method. In addition, by using this phase-shift encoding method, it is possible to produce spatially unresolved measurements of displacement or velocity distributions (propagators) characterizing the flow of liquid in a porous medium (Lebon et al., 1996; Packer and Tessier, 1996; Seymour and Callaghan, 1997; Amin et al., 1997; Manz et al., 1999; Chang and Watson, 1999). Park and Gibbs (1999) have also recently considered the application of magnetic resonance to study fluid flow and dispersion in fixed beds of particles.

In a previous article (Sederman et al., 1997) we presented 2-D MRI visualizations at 195 $\mu$m resolution, in two orthogonal planes, of liquid flow through two randomly packed beds

Correspondence concerning this article should be addressed to L. F. Gladden.

of glass ballotini. In a further article (Sederman et al., 1998) we extended this study to the analysis of the flow in a packed bed for which a full structural image of the bed was obtained along with MRI flow visualizations in six independent planes, perpendicular to the axis of the bed. In both articles, 3-D volume images of the beds were partitioned into individual pores, using an algorithm based on a variant of morphological thinning (Baldwin et al., 1996; Gladden and Alexander, 1996), and it was shown that there existed substantial heterogeneity in flow within the bed, with approximately 10% of the pores carrying 40% of the total volumetric flow and large regions containing virtually stagnant fluid. Correlations between both the volumetric flow rate and the average fluid velocity within individual pores with various structural characteristics of the porous system, such as the radial position of the pore within the bed and its coordination (or connectivity) to other pores within the bed, were also presented. An important conclusion from this work was the need to introduce a local Reynolds number based on the flow within an individual pore and a scale-length given by the diameter of the pore to understand the pore-scale flow regimes within the bed.

In this article flow visualizations within the same packed bed as reported in earlier studies (Sederman et al., 1997, 1998) are presented for various flow rates and, hence, Reynolds numbers, spanning the introduction of inertial forces into creeping flow. Flow velocity was measured in a direction both parallel and perpendicular to that of superficial flow. Two Newtonian fluids with different viscosities (water and a 33.7% w/w glucose solution in water) were used. The data presented will demonstrate that while the gross features of the flow pattern scale approximately linearly with overall volumetric flow rate, for large regions of near-stagnant fluid the flow velocity does not scale in this way. It is also observed that transitions from creeping flow to inertial flow occur within specific pores at a local Reynolds number of approximately 30. The results obtained in the present study are contrasted to those of earlier studies (Mansfield and Issa, 1996; Seymour and Callaghan, 1997) which showed significant changes in the distribution of flow as a function of volumetric flow rate as well as hysteresis effects. It is suggested that this discrepancy is most likely due to incomplete saturation of the void space in this earlier work. Finally, the implications are considered of the results presented here. First, the approximate scaling of the flow pattern with volumetric flow rate which occurs despite a transition in the type of flow within individual pores can be understood by assuming that the pressure distribution within the bed is largely determined by the near-stagnant fluid, the distribution of which is intimately linked to the structure of the void space. Second, the observation that the increased flow rate (and, hence, Reynolds number) does not significantly influence the regions occupied by near-stagnant fluid within the bed, but does cause transitions in the flow characteristics within regions (pores) within the interparticle space which do carry significant fluid flow, suggests that the performance of the bed when used, for example, as a fixed-bed reactor, would give local mass-transfer characteristics typical of those associated with the local (pore-scale) Reynolds number as opposed to the Reynolds number calculated from the global (macroscopic) properties of the bed. Validation of this hypothesis is the subject of ongoing work.

## Experimental Studies

The details of the operation of the experimental flow loop and the MRI techniques employed are the same as that detailed in Sederman et al. (1997, 1998). For completeness however, a brief description is given here.

### *Construction and operation of the packed bed and flow loop*

A glass column of diameter 4.6 cm and length 70 cm was used to contain the bed. The bed was prepared by randomly packing the full height of the column with glass ballotini of 5 mm diameter. A section 40 cm above the bottom of the column was imaged thereby ensuring that the imaged velocity field is free from end effects. To form the bed, the column was filled with deionized water and the ballotini were immersed in deionized water. After ensuring that all surfaces were free of air bubbles, the ballotini were poured into the column and the top portion of the column was fitted to form a seal and prevent air from entering the system. The ends of the column were then fitted to two reservoirs, which both contained either water or the glucose solution (33.7% w/w glucose). During the experiment, the system was subject to an excess pressure of approximately 2 kPa to prevent air bubbles from forming.

A constant flow rate of either fluid through the packed bed was obtained by pumping the respective fluid from the lower reservoir to the upper reservoir using a variable-speed peristaltic pump. The pressure drop through the flow loop (piping and packed bed) was balanced by the difference in head between the two reservoirs, this being allowed to equilibrate before data acquisition began. All the experiments using water were first conducted, then the valves at the outlet and inlet to the column were closed, thus enabling the reservoirs to be detached. The contents of the reservoirs were replaced by the glucose solution and then reattached to the valves at both ends of the column. This procedure ensured that identically positioned slices of the column were imaged in all experiments.

### *MRI flow visualizations*

The magnetic resonance visualizations of the bed structure and fluid flow were performed using a Bruker Spectrospin DMX 200 NMR spectrometer with a 4.77 T, 15 cm bore vertical magnet equipped with shielded gradient coils providing a maximum gradient strength of 13.9 G/cm. A bird-cage radio-frequency coil of diameter 6.3 cm, length 6 cm, and tuned to 199.98 MHz for the $^1$H resonance was used. Both the water and glucose solutions were doped with copper (II) sulphate, in order to reduce their respective spin-lattice relaxation times ($T_1$) to 600 ms, hence, decreasing data acquisition time.

A detailed treatment of the MRI techniques used in this work can be found in Callaghan (1991), while specific applications of NMR and MRI in chemical engineering have been reviewed by Gladden (1994). A review of applications of magnetic resonance to flowing systems has also recently been presented by Fukushima (1999). The basic velocity imaging pulse sequence used is shown in Figure 1, and is based on the velocity imaging technique of dynamic NMR microscopy

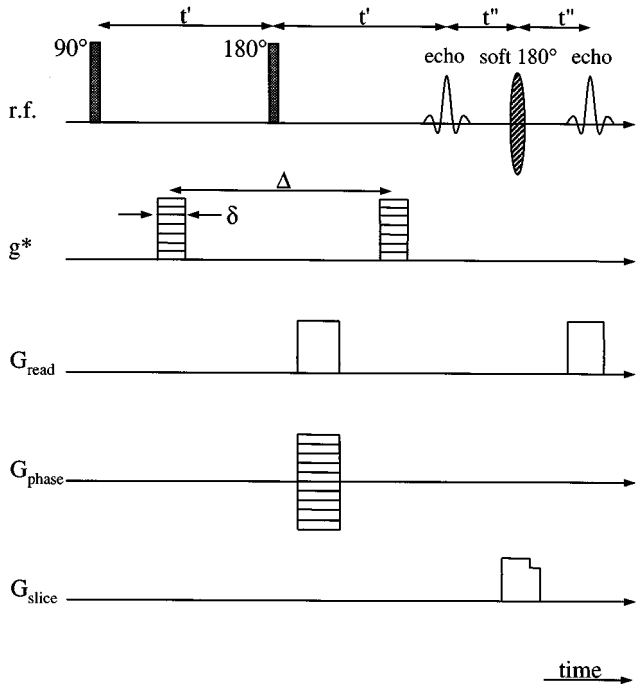


**Figure 1. MRI pulse sequence used to image the velocity field in a 2-D image slice.**

(Callaghan, 1991; Callaghan and Xia, 1991). The experiment requires two spatial dimensions and one velocity dimension. The velocity information is encoded for each voxel in each of the two spatial dimensions by applying velocity encoding gradients ($g^*$) which induce a phase shift that is determined by the displacement of the spins over the time-scale, $\Delta$. A $^1$H 90° pulse of duration 92 $\mu$s was used to irradiate the sample, the signal from this being refocused in succession by a hard 180° pulse of duration 184 $\mu$s and a soft 180° pulse of duration 800 $\mu$s, thereby exciting a 1 mm thick slice. The final data matrix consisted of $256\times256$ spatial points by 12 velocity points; given the selected field-of-view was 50 mm, the in-plane spatial resolution was therefore 195 $\mu$m$\times$195 $\mu$m. The repetition time was 600 ms. The read and phase gradients were applied for 1.9 ms; a read gradient of 4.65 G/cm was used, with a maximum value of 2.61 G/cm in the phase direction. The duration of the velocity encoding gradients ($\delta$) was varied between 3.7 and 1.7 ms and the spacing between them ($\Delta$) was varied between 30 and 18 ms, in order to produce a range of velocity measurement suitable for the particular flow rate being measured and to minimize any wraparound problems in the phase measurements. The velocity gradient, $g^*$, was incremented in 12 equal steps from 1.4 G/cm to a maximum of 13.9 G/cm. The direction of the velocity encoding gradient was changed to measure the magnitudes of the velocity in two perpendicular directions; parallel and perpendicular to the direction of superficial flow. These data were acquired for image slices both parallel and perpendicular to the direction of superficial flow. A slice gradient of 3.5 G/cm was used, of duration 1.8 ms, with an additional refocusing gradient of duration 1 ms. To establish the zero of velocity, velocity images of stationary water in the packed bed were acquired. These images were also used to correct for phase shifts in the images induced by eddy currents when velocity was measured in either the read or phase direction. The MRI frequency spectrum of the glucose solution contained a second smaller peak due to the glucose which had a short spin-spin relaxation time ($T_2$) of less than 10 ms. By employing an echo time in excess of 30 ms in the r.f. pulse sequence, chemical shift artefacts in the flow visualizations were avoided.

The maximum fluid velocity observed in the in-plane direction is approximately 10 mm/s. Between the application of the velocity encoding gradients the small fraction of spins with this maximum velocity will have travelled a distance (180 $\mu$m for $\Delta = 18$ ms) comparable to the in-plane voxel size (195 $\mu$m). The temporal delay between velocity encoding gradients therefore results in a velocity-dependent spatial averaging in the velocity image. Hence the in-plane resolution actually achieved will be less than 195 $\mu$m in regions of high flow velocity and may be of order 360 $\mu$m in the worst case. This effect does not influence our conclusions since the quantitative analysis presented involves averaging over pore-scale elements of volume which are typically 10–20 voxels in diameter.

A 3-D volume image was also acquired of the packed bed when it contained only stationary water, using a conventional 3-D spin-echo imaging sequence. The repetition time and echo time used were 800 ms and 6.3 ms, respectively. The read and phase gradients were applied for 1.5 ms, a read gradient of 4.65 G/cm was used with a maximum gradient strength of 2.0 G/cm in both phase directions. The 3-D data matrix consisted of $256\times128\times128$ points; giving a resolution of $195\times390\times390$ $\mu$m$^3$. This data set was zero-filled in the two phase-encoding directions prior to Fourier transformation so that the resulting image consisted of cubic voxels of size $195\times195\times195$ $\mu$m$^3$, to facilitate the further analysis.

### *Characterization of materials*

The viscosities of the glucose solution and water used in the experiments were measured with a Contraves L530 Low Shear 30 Viscometer over a range of strain rates from 3.23 to 27.7 s$^{-1}$. Both solutions were found to be Newtonian. A glucose solution of concentration 33.7% w/w was used, which had a viscosity ($\mu$) of $3.89\times10^{-3}$ Pa·s and a density ($\rho$) of 1,090 kg/m$^3$. The viscosity of the pure water was found to be $0.95\times10^{-3}$ Pa·s and its density to be 1,001 kg/m$^3$. A series of flow visualizations were conducted using flow rates of 1, 2 and 4 cm$^3$/s for water and 1, 4 and 8 cm$^3$/s for the glucose solution. These flow rates corresponded to Reynolds numbers ($v\rho2a/\mu$), where $a$ is the radius of the packing particles (2.5 mm) and $v$ is the superficial velocity, of 3.63, 7.26, 14.52 for water and 0.84, 3.38, 6.75 for the glucose solution.

## Data Analysis

The 3-D image of the water-saturated packed bed was first partitioned into individual pores using an in-house algorithm based on a variant of the morphological thinning technique (Baldwin et al., 1996; Gladden and Alexander, 1996). In this algorithm a single pore is defined as a portion of the pore space bounded by solid surfaces and planes erected where the hydraulic radius of the pore space exhibits local minima.

Analysis of the flow visualization data recorded for the component of the flow velocity in the direction of superficial flow, for all image slices acquired perpendicular to the direction of superficial flow, proceeded as follows. The 12 velocity data points for each voxel in the image plane, were first zero-filled in the velocity dimension prior to Fourier transformation to provide 256 points in the velocity domain ($Z$). A simple exhaustive search algorithm was then applied to $Z$ to determine both the position of the maximum in signal intensity in the velocity domain for each voxel, which corresponds to the velocity of the fluid within the voxel, and the full-width at half maximum (FWHM) of this signal which is related to the diffusivity of the fluid (Callaghan, 1991). Wraparound of the phase can lead to wraparound of the velocity so that a voxel in which the flow has a large positive velocity will contain a value indicating a large negative flow velocity. Such

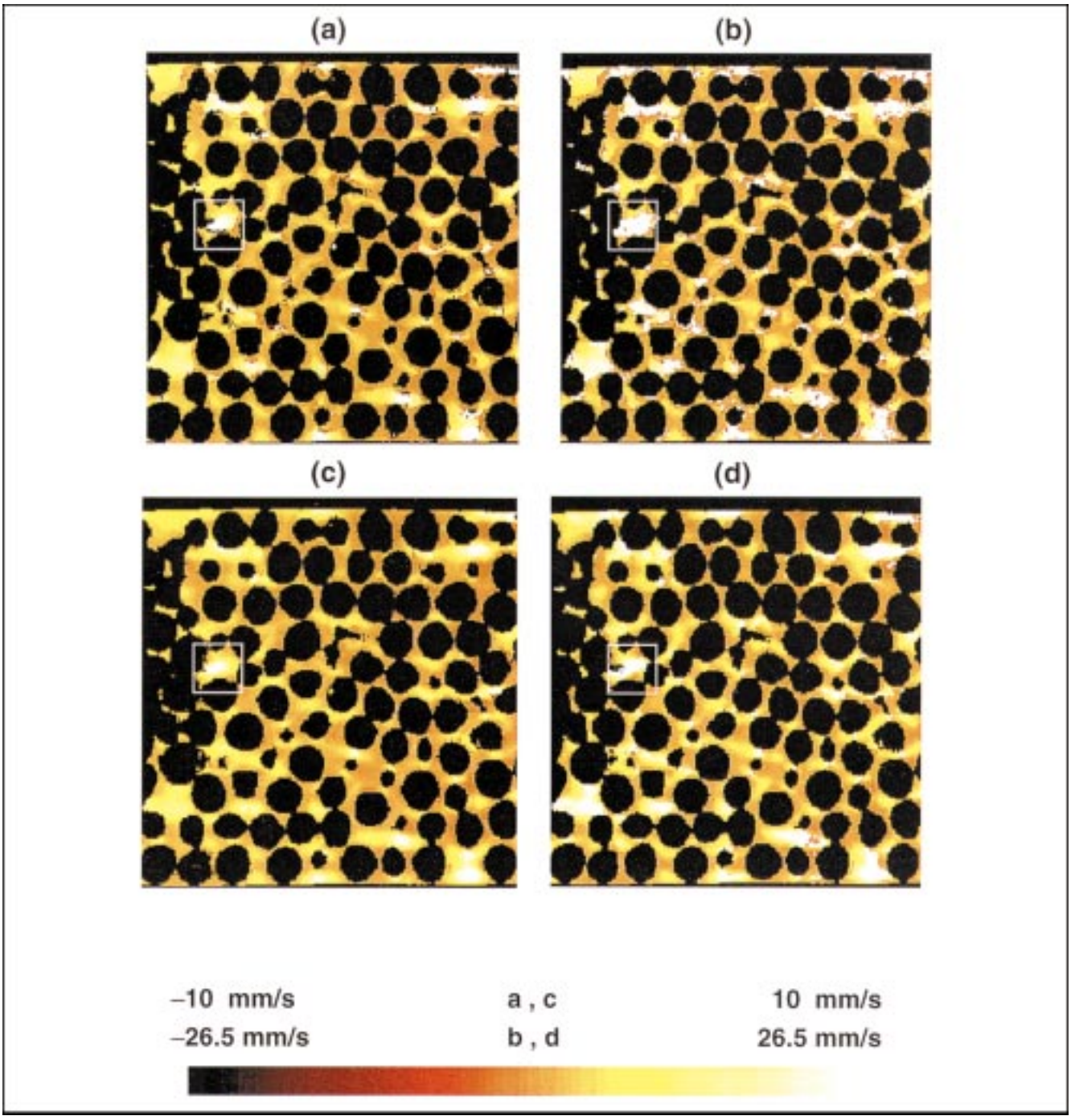


**Figure 2. Component of velocity in the superficial flow direction for an image slice parallel to the axis of the column.**

The direction of superficial flow is from left to right in the images and is indicated as a positive quantity. Images acquired for water at a flow rate of (a) 1 $cm^3/s$ and (b) 4 $cm^3/s$, and glucose solution at a flow rate of (c) 1 $cm^3/s$ and (d) 4 $cm^3/s$ are shown.

voxels are readily identified and corrected by requiring the flow field to be locally continuous. Prior to analysis, the image was first gated, to ensure that the algorithm was only applied to voxels for which signal intensity in the $Z$ domain was above a certain threshold, in this way the contribution of noise to the data was eliminated in the subsequent analysis. The data were then corrected for zero flow offsets and a mask of the 2-D image of the slice of interest was then applied such that signal intensity associated with voxels which did not contain water was set to zero. Having defined the individual pores constituting the porous medium by application of the image analysis algorithm as discussed earlier, the volumetric flow rate through each pore $q_{zj}$ was then calculated as defined.

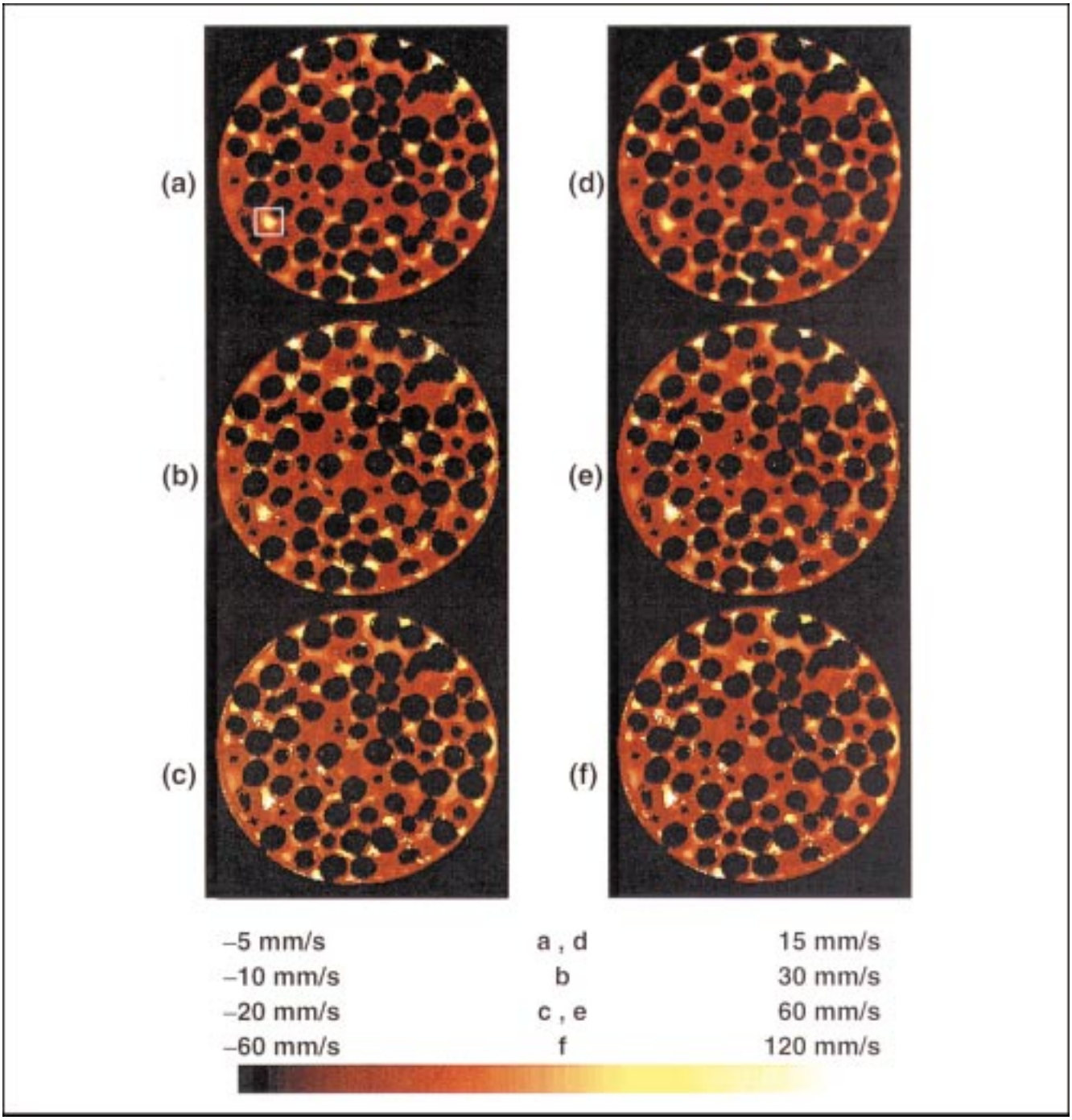


**Figure 3. Component of velocity in the superficial flow direction for an image slice perpendicular to the axis of the column.**

The direction of superficial flow is out of the page, and is indicated as a positive quantity. Images acquired for water at a flow rate of (a) 1 $cm^3/s$ , (b) 2 $cm/s$ , (c) 4 $cm^3/s$, and glucose solution at a flow rate of (d) 1 $cm^3/s$, (e) 4 $cm^3/s$, (f) 8 $cm^3/s$ are shown.

$$q_{zj} = \int_{\text{pore},\,j} u_{zj}\, dS_j = A \sum_{\text{pore}\,j} u_{zji} \qquad (1)$$

where $q_{zj}$ is the volumetric flow rate through the pore $j$ in an axial direction (the direction of the superficial flow), $u_{zj}$ is the velocity in the axial direction, and $dS_j$ is an element of area perpendicular to the axis of the bed. The integral is replaced by a summation over all voxels forming the cross section of the pore where $A$ is the area of one face of a cubic voxel and $u_{zji}$ is the flow velocity in the axial direction for voxel $i$ in pore $j$.

## Results

### *Influence of flow rate and Reynolds number on the distribution of flow within the bed*

In Figure 2 velocity images are presented for the same slice parallel to the axis of the column, taken through the center of the column; the direction of superficial flow is from left to right in these images. The experimental conditions for each image are: water at a flow rate of (a) 1 $cm^3/s$, and (b) 4 $cm^3/s$, and glucose solution at a flow rate of (c) 1 $cm^3/s$ and (d) 4 $cm^3/s$. Figure 3 shows typical velocity images for a slice perpendicular to the axis of the column, the direction of superficial flow being out of the page in these images, for water at a flow rate of (a) 1 $cm^3/s$, (b) 2 $cm^3/s$ and (c) 4 $cm^3/s$ and for glucose solution at a flow rate of (d) 1 $cm^3/s$, (e) 4 $cm^3/s$ and (f) 8 $cm^3/s$. The assignment of individual pores within the interparticle space for the image slice shown in the velocity images (Figure 3) is shown in Figure 4. A feature that is immediately obvious in both Figures 2 and 3 is the heterogeneity of local flow conditions, with large regions of essentially stagnant fluid. This observation is consistent with our earlier results which have been discussed in detail elsewhere (Sederman et al., 1997, 1998). However, perhaps the most striking feature in both sets of images is the similarity in the heterogeneity of the velocity fields within a given image slice; that is, over the length-scale of the bed. Regions or pores of comparatively high flow rate and stagnation occur at identical locations within the bed indicating that the bed-scale flow pattern established through the pore space is independent of both flow rate and Reynolds number over the range of conditions investigated. Furthermore, the flow patterns are reestablished when the flow is first stopped and then restarted, indicating that hysteresis effects are not apparent in the flow.

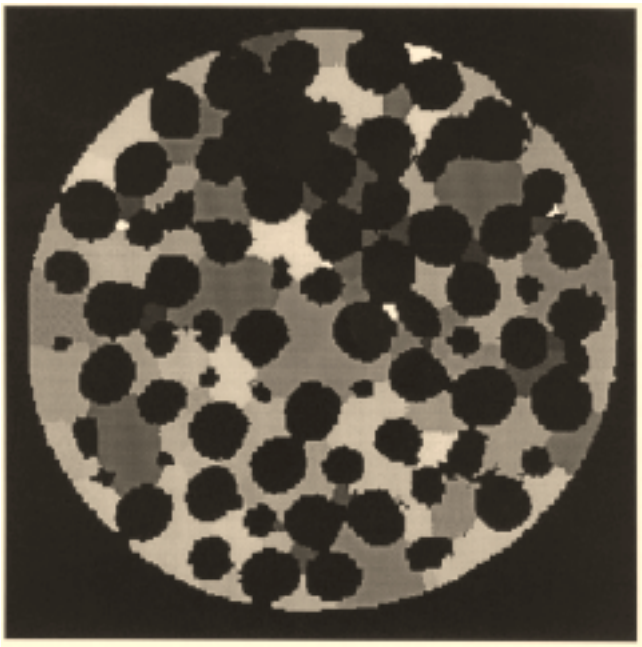

**Figure 4. 2-D image corresponding to the image slice, as shown in Figure 3.**

The interparticle space has been divided into separate pores, indicated by regions of different shading, using an image-analysis procedure based on a variant of morphological thinning in which boundaries between pores are defined as minima in the hydraulic radius of the pore space.

Kutsovsky et al. (1996), using a similar experimental design, found considerably less heterogeneity in the bed-scale flow pattern than is observed in the present work. This difference is likely to be attributable to the structure of the packing and, hence, pore space. Kutsovsky et al. (1996) used a consolidated packing in a bed of column-to-particle diameter ratio 6·6, whereas the results reported here are for an unconsolidated packing in a bed of column-to-particle ratio 9·2. The packing and, hence, pore structure in the work of Kutsovsky et al. is therefore likely to be more ordered than that of the present work.

Velocity distributions, for flow in the superficial flow direction, derived from all voxels in the velocity images in Figure 3 are shown for both water and the glucose solution for flow rates of 1 and 4 $cm^3/s$ in Figures 5a and 5b respectively. Figure 5c shows the evolution in the velocity distribution for water as flow rate is increased. It is seen in Figures 5a and 5b that, for a given flow rate, the data for water and the glucose solution are very similar, indicating that the flow is (statistically) unaffected by the change in viscosity and, hence, Reynolds number. With reference to Figure 5c, as the flow rate is increased the number of voxels associated with essentially stagnant fluid is reduced and a substantial increase in the tail of the distribution to positive velocity is observed. Figure 6 shows the velocity distributions for both fluids for flow rates of 1 and 4 $cm^3/s$ for the same image slice as shown in Figure 3, where velocity is measured in a direction perpendicular to the direction of superficial flow, instead of parallel to it. As expected the velocity distributions are symmetric, centred upon zero velocity and the extent of dispersion in the flow, indicated by the width of the distribution, increases with increase in superficial velocity. Again, at the same flow rates, the two fluids are characterized by very similar velocity distributions. Also apparent in Figure 5 is the presence of some voxels with negative velocity, indicating countercurrent flow, in agreement with our earlier work (Sederman et al., 1997) and that of Kutsovsky et al. (1996). We note that the amount of countercurrent flow increases with the overall volumetric flow rate through the bed (Figure 5c).

The volumetric flow rate through each of the pores ($q_{zj}$ in Eq. 1) identified in Figure 4 was calculated for the six velocity images shown in Figure 3. In Figure 7 the value of the volumetric flow rate through each pore is plotted. In Figure 7a data for water at a flow rate of 1 $cm^3/s$ are plotted against those for glucose solution at a flow rate of 1 $cm^3/s$. In Figure 7b data for water at a flow rate of 1 $cm^3/s$ is plotted against data acquired for water at flow rates of 2 and 4 $cm^3/s$, re-

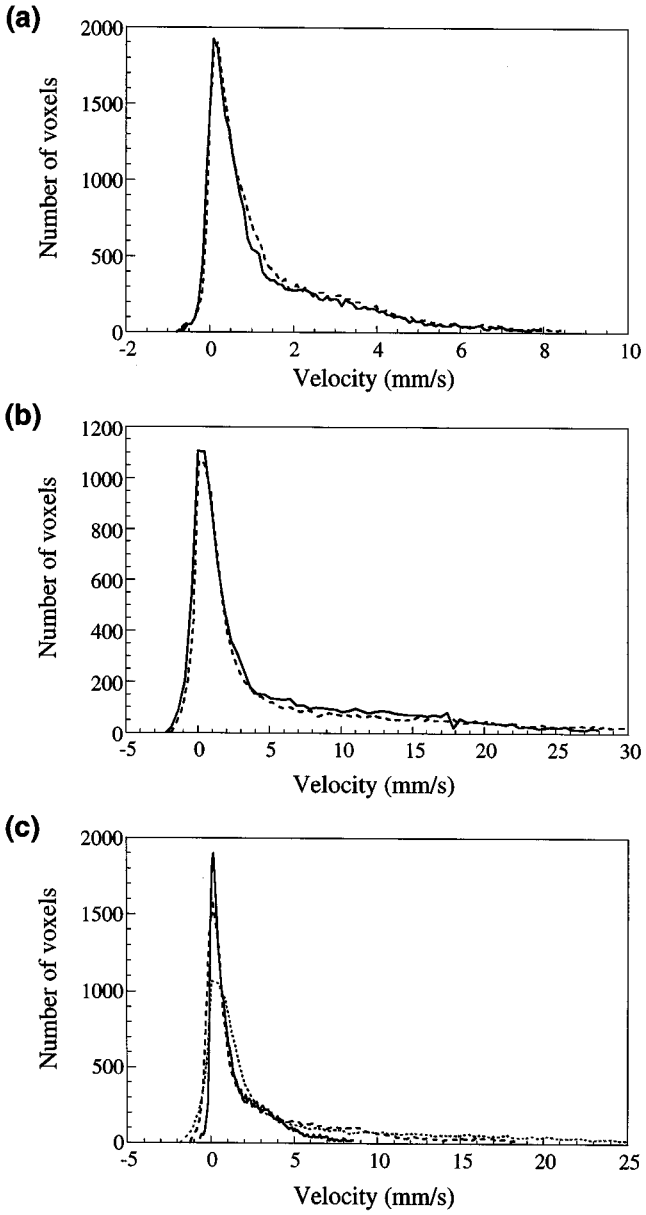


**Figure 5. Distributions of velocity in the superficial flow direction, on a voxel basis, for the two fluids investigated.**

(a) and (b) show data obtained for water (– – –) and the glucose solution (——) at flow rates of 1 and 4 $cm^3/s$ respectively. The distributions are remarkably similar. The evolution in the velocity distribution for water as flow rate is increased is shown in (c) for flow rates of 1 $cm^3/s$ (——), 2 $cm^3/s$ (– – –) and 4 $cm^3/s$ (· · · ·).

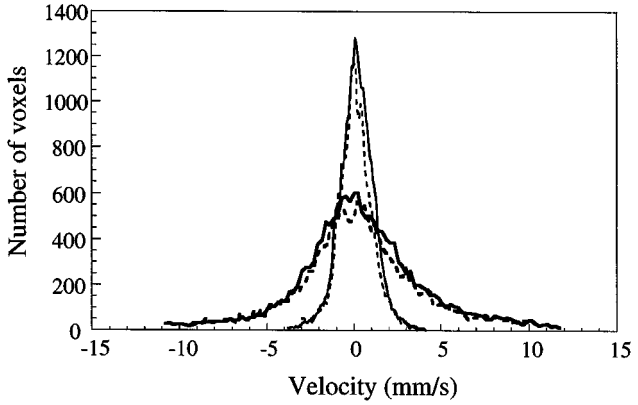


**Figure 6. Distribution of velocity in a direction perpendicular to that of the superficial flow, on a voxel basis.**

Data are presented at flow rates for glucose solution of 1 $cm^3/s$ (——) and 4 $cm^3/s$ (——) and for water at 1 $cm^3/s$ (– – –) and 4 $cm^3/s$ (– – –). At corresponding flow rates the distributions are remarkably similar. As expected the distributions are symmetric and centered upon zero.

spectively. In Figure 7c data sets of approximately comparable Reynolds number are compared: water at a flow rate of 1 $cm^3/s$ ($Re = 3.63$) is compared with glucose solution at a flow rate of 4 $cm^3/s$ ($Re = 3.38$); and water at a flow rate of 2 $cm^3/s$ ($Re = 7.26$) is compared with glucose solution at a flow rate of 8 $cm^3/s$ ($Re = 6.75$).

Inspection of Figures 2 and 3 and the pore-to-pore comparison presented in Figure 7 suggests that changing overall volumetric flow rate or Reynolds number does not significantly change the overall flow distribution within the bed, and that the local flow velocity scales approximately linearly with the volumetric flow rate. However, this scaling does not apply to the near-stagnant fluid. Figure 5c shows that the overall velocity distribution does not simply scale with volumetric flow rate; in particular the large peak representing near-stagnant flow broadens but does not shift to higher flow rates. The slope of the linear fit in Figures 7a–7c reflects the ratio of the bulk flow rates and the values so-obtained deviate by less than 4% from the corresponding ratio of experimentally-determined bulk flow rates. The linear scaling apparent for the pores associated with high flow rates becomes less good for pores associated with low flow rates. This observation is consistent with the observations made above concerning the histograms of flow velocity (Figure 5); near-stagnant flow does not scale linearly with the overall volumetric flow rate.

### *Influence of flow rate and Reynolds number on pore-scale flow patterns*

In the images shown in Figures 2 and 3, corresponding to both water and glucose solution, it is observed that pores associated with relatively high flow velocities exhibit more abrupt velocity changes at their periphery relative to the flow through the center of the pore, as the flow rate and consequently Reynolds number are increased. Such effects are clearly seen, for example, in the pore indicated in Figure 2. In Figure 8a, velocity profiles for the pore indicated in Figure 3a are shown. The velocity profile across this pore, passing through the maximum velocity within the pore, was determined for all six velocity images shown in Figure 3. In Figures 8b and 8c the same profiles are shown for water and the glucose solution, respectively, normalized to the maximum velocity through the pore. With increasing Reynolds number the velocity profiles develop a flatter profile towards the center of the pore, and an increasing gradient in the velocity of the fluid close to the solid surface.

According to Rode et al. (1994), the range of Reynolds numbers investigated here (0.84–14.52) spans the transition

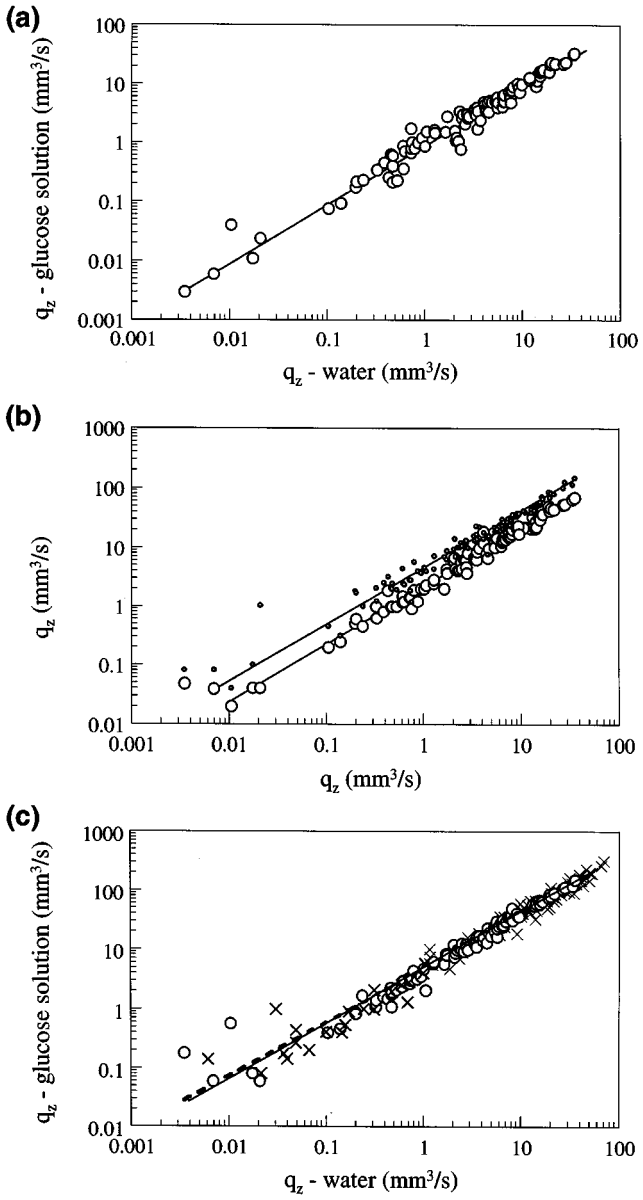


**Figure 7. Flow rate through each pore in Figure 4 for corresponding pores for the following flow rates.**

(a) water, 1 $cm^3/s$ versus glucose solution, 1 $cm^3/s$ (○); (b) water, 1 $cm^3/s$ versus water, 2 $cm^3/s$ (○) and water, 4 $cm^3/s$ (·) respectively; (c) water, 1 $cm^3/s$ versus glucose solution, 4 $cm^3/s$ (○); and water, 2 $cm^3/s$ versus glucose solution, 8 $cm^3/s$ (×). The best linear fits to these data are also shown, the magnitude of the gradients being: (a) 0.96; (b) (○) 2.04, (·) 3.97 and (c) (○) 3.98, (×) 3.91. These slopes reflect the ratio of the experimentally-determined bulk flow rates to within an accuracy of 4%.

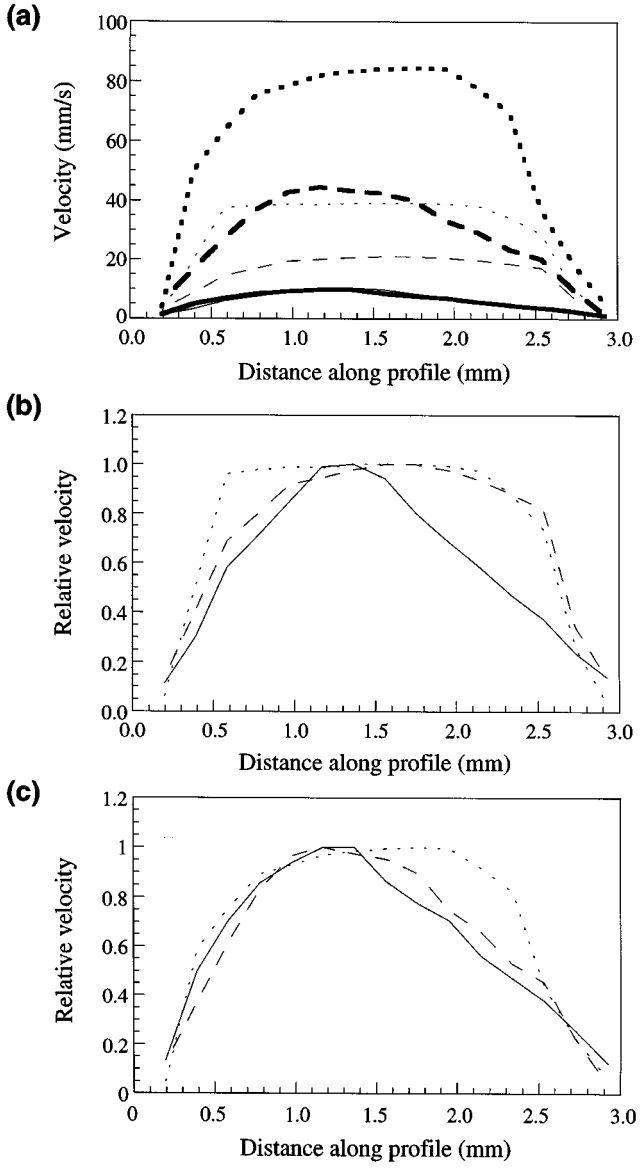


**Figure 8. Velocity profiles through a single pore.**

(a) Velocity profile through the point of maximum velocity for the pore identified in Figure 3a for each image in Figures 3a–3f. Data are shown for water at a flow rate of: 1 $cm^3/s$, $Re = 3.63$ (——); 2 $cm^3/s$, $Re = 7.26$ (– – –); 4 $cm^3/s$, $Re = 14.52$ (– – – –); and for glucose solution at a flow rate of: 1 $cm^3/s$, $Re = 0.84$ (——); 4 $cm^3/s$, $Re = 3.38$ (– – –); 8 $cm^3/s$, $Re = 6.75$ (------. The profiles shown in (a) are shown again in (b) and (c), normalized to the maximum velocity within each profile. The data for water are shown in (b): 1 $cm^3/s$ (——), 2 $cm^3/s$ (– – –), 4 $cm^3/s$ (-----). The data for the glucose solution are shown in (c): 1 $cm^3/s$ (——) , 4 $cm^3/s$ (– – –), 8 $cm^3/s$ (-----) .

from the creeping flow regime to a steady, nonlinear flow regime, characterized by a variable thickness viscous sublayer, adjacent to the solid particles, and an inertial core. Such a transition has been reported by Liu et al. (1994), from experimental observations, to occur at a Reynolds number between 1.6 and 3.5. However, if wall effects introduced by the column are accounted for, the same authors suggest a transition at a Reynolds number of approximately 4. In creeping flow, a flow profile extracted from a short cylindrical pore would have a parabolic shape. As Reynolds number is increased and inertial forces become more significant, the inertial core will grow and the velocity profile flatten at its maximum, resembling that characteristic of laminar flow at the entrance to a pipe (Rode et al., 1994). The velocity profiles shown in Figure 8 follow this trend; an inertial core develops

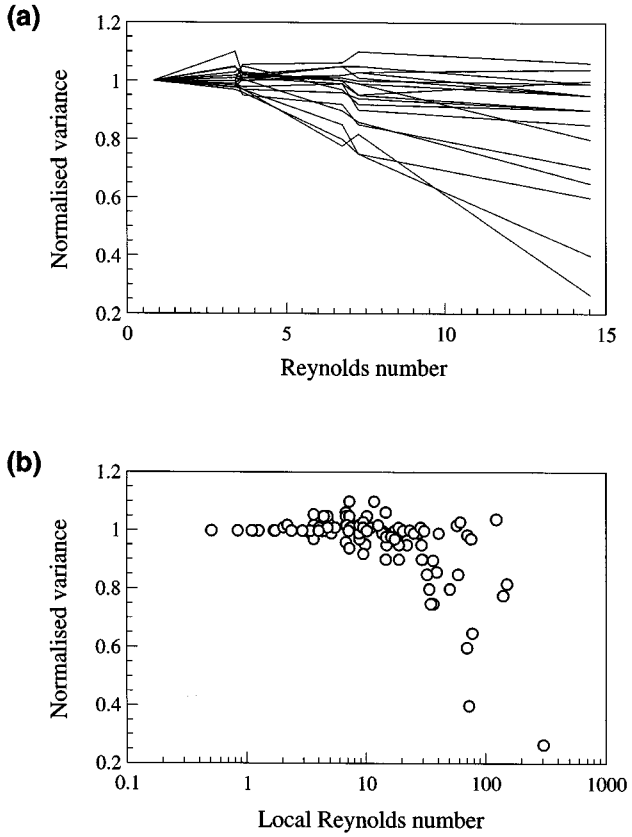


**Figure 9. (a) Change in variance of 18 randomly selected velocity profiles extracted from pores identified in the flow visualizations in Figures 3a–3f; (b) the same data are plotted as a function of a local Reynolds number (Eq. 2).**

(a) Each line shows how variance evolves as Reynolds number is increased for a particular pore. The variance has been normalized for each pore relative to that which existed at the lowest Reynolds number considered (0.84) to aid comparison between the various pores. (b) A transition occurs at a value of the local Reynolds number of approximately 30, indicating the development of an inertial core in the velocity profiles.

at lower flow rates for water than for glucose, as is to be expected given the relative viscosities of the two fluids.

To quantify these observations of the shape of the velocity profile we define the variance of the shape of the normalized velocity profile (Figures 8b and 8c) as the sum of differences squared between each point in the profile and the maximum in the profile (which is always 1.0), divided by the number of points in that profile. As the inertial core grows in these profiles and the shape of the curve is flattened around the maximum, the value of variance defined in this way, should decrease. The change in variance is shown in Figure 9 for velocity profiles extracted from 18 randomly selected pores from the images shown in Figure 3. Each line shows the change in variance for each pore plotted as a function of Reynolds number. To aid comparison, the values of variance for each of the profiles have been normalized relative to the variance which existed at the lowest Reynolds number (0.84) for each of the profiles. The variance for the majority of the profiles remains approximately constant. However, a few pores experience a marked drop in variance which is strong evidence of a developing inertial core. There is no sudden, uniform transition from viscous boundary-layer dominated flow across the bed as Reynolds number increases; instead, flow within individual pores within the bed undergoes a transition from viscous-dominated flow to inertial flow.

For each velocity profile used to construct Figure 9a, a local Reynolds number is defined as in Sederman et al. (1998)

$$\frac{d\rho v_{\text{av}}}{\mu}, \tag{2}$$

where $d$ is the length of the velocity profile (that is, the pore diameter) and $v_{\text{av}}$ is the average velocity calculated from that profile. The normalized variance shown in Figure 9a is plotted against this local Reynolds number for each profile in Figure 9b. A sharper transition is now evident in the slope of the variance as a function of local Reynolds number, occurring at a value of the local Reynolds number of approximately 30. We can therefore associate a local Reynolds number of $\sim 30$ as a critical value for the pore-scale transition from viscous-dominated flow to inertial flow. There is still a certain amount of scatter in Figure 9b, which is not surprising given the approximate determination of the local Reynolds number and the crude model adopted for this analysis. A better estimate of the local Reynolds number may, for example, be achieved by considering the local geometry of the pore space and by defining both the velocity profile and local Reynolds number using measurements perpendicular to the local velocity vector. Such an analysis would require fully three-dimensional flow visualization and is beyond the scope of this article.

## Discussion

There are two particular points of discussion which arise from this work. First, the similarity in the heterogeneity of the flow pattern on the scale of the whole bed for the range of flow rates and Reynolds number studied. Second, the observation of local transitions in the flow from creeping flow to flow characterized by an inertial core which occurs at a critical local Reynolds number of approximately 30. Both these points will now be discussed in turn.

### *Flow behavior as a function of changing volume flow rate and Re*

The consistency in the bed-scale flow pattern with changing volumetric flow rate and Reynolds number observed in this work is in contrast to the observations of both Mansfield and Issa (1996) and Seymour and Callaghan (1997). Both these studies obtained two dimensional velocity images of flow within porous systems using essentially the same MRI technique as used in our work to measure velocity, that is, phase-shift encoding. Mansfield and Issa (1996) used a rapid imaging technique on a porous Bentheimer sandstone, while Seymour and Callaghan (1997) investigated a packing of polymer spheres of diameter 90.7 $\mu$m. Both studies found that when the flow rate was increased, the flow field changed in terms of the spatial distribution of where the high and low flow rates were observed. However it should be noted that neither study imaged flow within individual pores, instead presenting

velocity images where the voxels encompassed a large number of packing particles and, hence, pores. Thus over the encoding time, $\Delta$, the water molecules sample a number of pores, and a degree of temporal averaging is introduced. To investigate the effects of voxel size, we have degraded the resolution of our velocity images so that the resolution relative to the pore size was similar to that reported in the studies of Seymour and Callaghan (1997) and Mansfield and Issa (1996). The consistency of the bed-scale flow pattern was still found in these low-resolution data.

Mansfield and Issa (1996) have proposed three possible reasons for the irreproducibility in the visualized flow fields obtained in their study. First, flow instabilities may occur during the transition from one steady state to another when the bulk flow rate is changed. Second, any change in the flow rate will cause a change in the saturation level of a given pore; that is, a change in the position and amount of air trapped in the pore space. Third, any movement, generated by the change in superficial flow rate, of fine particles confined between fixed grains of material will cause a physical modification of the pore space and, hence, an associated change in the flow field. Of these possible explanations, the movement of fines cannot account for the results of Seymour and Callaghan (1997) obtained for the bed formed from 97 $\mu$m spheres as no fines were present. Further, an argument based on flow instabilities is not supported by the present study since the pore size for both the sandstone and the bed formed from 97 $\mu$m spheres is considerably smaller than that considered here, and also the Reynolds number characterizing the flows considered in this work are higher than those studied in the other works. Since intrinsic flow instability increases with increasing Reynolds number, we would therefore expect any phenomenon associated with flow instabilities to be enhanced in the present study which is clearly not the case. Therefore, we conclude that the most likely explanation of the contrasting observations is that the void space of the systems studied in the earlier works was not completely water-saturated. Redistribution of air within the pore space with changes in the bulk flow parameters could then lead to the observed changes in flow distribution and hysteresis. While it was possible to completely remove air from our own experiments, this would be far more difficult to achieve in the case of the experiments performed with sandstone and, perhaps also, for the 97 $\mu$m spheres. In a future article we will report studies of a two-phase flowing system of water and air in packed beds of 5 mm diameter ballotini; these experiments reveal both considerable hysteresis and a dependence on flow rate in the bed-scale flow pattern. Such hysteresis in two-phase flow in a packed bed (trickle bed) system has also been reported by Wang et al. (1995).

### *Flow heterogeneity*

As discussed above a number of results are clear from the present work:

- The overall flow distribution within the bed does not change significantly with volumetric flow rate or Reynolds number.
- Except for the pores containing near-stagnant fluid there is a linear scaling of the mean flow through each pore as a function of the volumetric flow rate.
- Regions of near-stagnant flow remain so as the volumetric flow rate is increased; the scaling of flow velocity in these regions is not linear.
- There is a local transition at a local Reynolds number of approximately 30 from the creeping flow regime to a steady, nonlinear flow regime characterized by an inertial core.

Over the range of Reynolds number considered here a number of pores undergo the transition in flow behavior to show an inertial core as the volumetric flow rate is increased. However, although the flow pattern changes within such pores, the net flux through them simply scales linearly with volumetric flow rate. To reconcile these observations we note that a large volume fraction of the bed consists of fluid which is approximately stagnant. This near-stagnant fluid will inevitably determine the pressure distribution within the bed; and, further, the regions (pores) containing the near-stagnant fluid are determined directly from the geometry and topology of the void space. Once the pressure distribution is fixed in this way it is not surprising that, for a given pore which is associated with a significant fluid flow, despite a change in the detail of the flow pattern within the pore as volumetric flow rate increases, the net flow is linearly related to the overall volumetric flow rate. This means that the heterogeneity within the flow field increases with increasing volumetric flow rate; this is supported by the change in shape of the velocity distributions in the direction of the superficial flow (Figure 5) and the increased prominence of the tail of the velocity distribution as the volumetric flow rate is increased.

This heterogeneity means that only a relatively small fraction of the bed is involved in carrying the majority of the flow and that this is not changed as the flow rate is increased. An implication of this observation is that it is the pores within the interparticle space which do carry significant fluid flow which are most likely to determine the performance of the bed when used, for example, as a fixed-bed reactor. For example, local mass-transfer characteristics typical of those associated with the local (pore-scale) Reynolds number as opposed to the Reynolds number calculated from the global (macroscopic) properties of the bed might better explain the operation of the bed. Further, it is noted that the distribution of regions of near-stagnant flow is determined by the local structure of the bed (as discussed in Sederman et al., 1997) and therefore such heterogeneity will exist for all beds independent of column-to-particle diameter ratio.

## Conclusions

Velocity images are presented for two Newtonian fluids of different viscosity, water and a glucose solution, over a range of flow rates and, hence, Reynolds numbers. Over the range of conditions investigated, both fluids produced remarkably similar bed-scale flow fields with virtually identically located regions of stagnation and high velocity flow channels. This effect was shown quantitatively in comparative plots of volumetric flow rate through individual pores for the various overall volumetric flow rates and Reynolds numbers examined in this study. In all cases, except for those regions containing near-stagnant flow, the flow through a given pore scales linearly with the overall volumetric flow rate through the bed. This behavior is in contrast to results previously presented in the literature in which the distribution of flow

changes significantly with overall volumetric flow rate and also shows hysteresis effects. It is most likely that these differences can be accounted for by incomplete fluid-saturation of the void space in previous work.

The range of Reynolds number, based on particle diameter, investigated (0.84–14.52) covers the range over which we would expect inertial effects to become significant. This phenomenon is observed in the images; abrupt velocity changes at the periphery of pores associated with high flow velocity are observed as Reynolds number is increased. This effect results in a change in shape of the profiles of velocity across individual pores with increasing Reynolds number, from roughly parabolic to a shape which is flattened at its maximum due to the development of an inertial core. This transition depends critically upon the local Reynolds number of each pore.

The flow distribution within the bed is determined largely by the near-stagnant fluid; the majority of the void space contains fluid which has a low velocity and these pores remain associated with low flow velocity as the overall volumetric flow rate and Reynolds number are changed since their flow characteristics are determined by the local geometry and topology of the void space. Consequently this near-stagnant fluid largely determines the pressure distribution within the bed. The net flow rate through the minority of pores carrying the majority of the flow is observed to scale linearly with the overall volumetric flow rate, as would therefore be expected. The inherent heterogeneity within the flow field is therefore increased as the overall volumetric flow rate is increased. This is seen directly in the histograms of the velocity distribution in the direction of the superficial flow. This heterogeneous flow pattern will have important implications on the effectiveness of the packed bed in practical situations and on the scaling behavior of the properties of the bed with total volumetric flow.

## Acknowledgments

LFG wishes to thank the EPSRC for the award of the NMR spectrometer. ASB, MLJ and AJS wish to thank the EPSRC, Cambridge Commonwealth Trust, and Shell for financial support, respectively.

## Notation

$a$ = radius of ballotini
$A$ = area
$d$ = length of a velocity profile across a pore
$D$ = diffusion constant
$g^*$ = velocity encoding gradient
$J$ = total number of pores
$Q$ = volumetric flow rate through the packed bed
$q_z$ = volumetric flow rate through a single pore in the direction of superficial flow
$S_j$ = cross-sectional area perpendicular to the axis of the bed
$T_1$ = spin-lattice relaxation time
$T_2$ = spin-spin relaxation time
$t'$ = pulse program timing
$t''$ = pulse program timing
$u_z$ = fluid velocity in direction of superficial flow
$v$ = superficial velocity (Q/A)
$v_{av}$ = average velocity
$Z$ = velocity domain in dynamic NMR microscopy
$\Delta$ = pulse program timing
$\delta$ = pulse program timing
$\mu$ = viscosity
$\rho$ = density

### *Subscripts*

$i$ = voxel, $i$
$j$ = pore, $j$
$z$ = component in direction of superficial flow

## Literature Cited

Amin, M. H. G., S. J. Gibbs, R. J. Chorley, K. S. Richards, L. D. Hall, and T. A. Carpenter, ''Study of Flow and Hydrodynamic Dispersion in a Porous Medium using Pulsed-Field-Gradient Magnetic Resonance,'' *Proc. Roy. Soc. Lond., Series A*, **453**, 489 (1997).

Baldwin, C. A., A. J. Sederman, M. D. Mantle, P. Alexander, and L. F. Gladden, ''Determination and Characterisation of the Structure of a Pore Space from 3D Volume Images,'' *J. Colloid Interface Sci.*, **181**, 79 (1996).

Callaghan, P. T., *Principles of Nuclear Magnetic Resonance Microscopy*, Oxford University Press, New York (1991).

Callaghan, P. T., and Y. Xia, ''Velocity and Diffusion Imaging in Dynamic NMR Microscopy,'' *J. Magn. Reson.*, **A91**, 326 (1991).

Chang, C. T. P., and A. T. Watson, ''NMR Imaging of Flow Velocity in Porous Media,'' *AIChE J.*, **45**, 437 (1999).

Fukushima, E., ''Nuclear Magnetic Resonance as a Tool to Study Flow,'' *Annu. Rev. Fluid Mech.*, **31**, 95 (1999).

Gladden, L. F., ''Nuclear Magnetic Resonance in Chemical Engineering: Principles and Applications,'' *Chem. Eng. Sci.*, **49**, 3339 (1994).

Gladden, L. F., and P. Alexander, ''Applications of Nuclear Magnetic Resonance Imaging in Process Engineering,'' *Meas. Sci. Technol.*, **7**, 423 (1996).

Kutsovsky, Y. E., L. E. Scriven, H. T. Davis, and B. E. Hammer, ''NMR Imaging of Velocity Profiles and Velocity Distributions in Bead Packs,'' *Phys. Fluids*, **8**, 863 (1996).

Lebon, L., J. Leblond, J.-P. Hulin, N. S. Martys, and L. M. Schwartz, ''Pulsed Field Gradient NMR Measurements of Displacements under Flow in Sphere Packings,'' *Magn. Reson. Imag.*, **14**, 989 (1996).

Liu, S., A. Afacan, and J. Masliyah, ''Steady Incompressible Laminar Flow in Porous Media,'' *Chem. Eng. Sci.*, **49**, 3565 (1994).

Mansfield, P., and B. Issa, ''Fluid Transport in Porous Rocks. 1. EPI Studies and a Stochastic Model of Flow,'' *J. Magn. Reson.*, **A122**, 137 (1996).

Manz, B., P. Alexander, and L. F. Gladden, ''Correlations Between Dispersion and Structure in Porous Media Probed by Nuclear Magnetic Resonance,'' *Phys. Fluids*, **11**, 259 (1999).

Nesbitt, G. J., A. de Groot, T. W. Fens, and J. H. M. Bonnie, ''Toward Validation of Porous Media Models using NMR Imaging and Image Analysis Techniques,'' *Magn. Reson. Imaging*, **9**, 779 (1991).

Packer, K. J, and J. J. Tessier, ''The Characterisation of Fluid Transport in a Porous Solid by Pulsed Gradient Stimulated Echo NMR,'' *Mol. Phys.*, **87**, 267 (1996).

Park, J., and S. J. Gibbs, ''Mapping Flow and Dispersion in a Packed Column,'' *AIChE J.*, **45**, 655 (1999).

Rajanayagam, V., Y. Shenggen, and J. M. Pope, ''Quantitative Magnetic Resonance Flow and Diffusion Imaging in Porous Media,'' *Magn. Reson. Imaging.*, **13**, 728 (1995).

Rode, S., N. Midoux, M. A. Latifi, A. Storck, and E. Saatdjian, ''Hydrodynamics of Liquid Flow in Packed Beds: An Experimental Study using Electrochemical Shear Rate Sensors,'' *Chem. Eng. Sci.*, **49**, 889 (1994).

Sederman, A. J., M. L. Johns, A. S. Bramley, P. Alexander, and L. F. Gladden, ''Magnetic Resonance Imaging of Liquid Flow and Pore Structure Within Packed Beds,'' *Chem. Eng. Sci.*, **52**, 14, 2239 (1997).

Sederman, A. J., M. L. Johns, P. Alexander, and L. F. Gladden, ''Structure-Flow Correlations in Packed Beds,'' *Chem. Eng. Sci.*, **53**, 2117 (1998).

Seymour, J. D., and P. T. Callaghan, ''Generalized Approach to NMR Analysis of Flow and Dispersion in Porous Media,'' *AIChE J.*, **43**, 2096 (1997).

Wang, R., Z. S. Mao, and J. Chen, ''Experimental and Theoretical Studies of Pressure Drop Hysteresis in Trickle Bed Reactors,'' *Chem. Eng. Sci.*, **50**, 2321 (1995).

*Manuscript received July 15, 1999, and revision received May 24, 2000.*